

Modeling and Control of Radial Force in Switched Reluctance Motor

Feng-Chieh Lin and Sheng-Ming Yang
Department of Mechanical and Electro-mechanical Engineering
Tamkang University, Taiwan
e-mail: smyang@mail.tku.edu.tw

Abstract—Unbalanced radial force acting on a rotor shaft is undesirable because it causes motor vibrations. Yet, motor vibrations can be reduced with intentionally produced shaft radial force which cancels the existing unbalanced radial forces due to a non-uniform air gap or external load. Due to its special structure, the shaft radial force and torque of a switched reluctance motor can be separately controlled when all pole currents are controlled independently. However, control of SRM radial force is rarely discussed in existing literature. This paper presents a scheme that produces a controlled radial force for a 12/8 pole SRM. In this scheme, mutual inductances between stator poles are included in the control model. The motor torque is controlled with the conventional method, i.e. all poles in the conduction phase are energized with the same current to produce the desired torque. Two extra poles from the descending- inductance phase are energized to produce the desired radial force. The cross-coupling torque produced by the force producing poles is compensated. The experimental results have verified that when controlled with the proposed scheme, the SRM was able to produce a controlled radial force when at standstill or running, and subjected to a load torque.

Keywords: Switched reluctance motor, Radial force control.

I. INTRODUCTION

Switched reluctance motors (SRM) develop torque through an interaction between the electromagnetic excitation from the stator poles and the rotor teeth. Once a particular combination of phase currents is established and maintained in the stator, the rotor teeth will be attracted into alignment with the stator poles in a particular position. This attraction force can be divided into tangential and radial force components relative to the rotor. The tangential force is converted into the rotational torque. The net radial force is generally zero due to the geometrically balanced motor structure. Unbalanced radial force acting on a rotor shaft is undesirable because it causes motor vibrations. For instance, in applications in which the external load is not balanced, or when the rotor is not centered causing a non-uniform air gap, shaft radial force exists [1-3]. For most motors, radial force cannot be changed after the motor is assembled. This radial force will be absorbed by the bearings and the load connected to the rotor. Due to its special structure and the way torque is produced, the SRM offers a unique opportunity to control shaft radial force without disrupting the normal rotational torque. It is possible to produce the radial force required to cancel the forces due to non-uniform air gap or external load, and consequently reduce motor vibrations.

Several methods have been proposed to produce controlled radial force for SRM. A radial force and torque decoupling control scheme has been proposed for 'self-bearing' control of a 12/8 pole SRM [4-7]. In the motor each stator pole contains a main and an auxiliary winding.

The main winding is used to control the motor torque. The auxiliary winding produces radial force for rotor levitation. This controller has a complicated implementation because of the required number of windings and computations. There were a number of reports that discussed using sinusoidal current waveforms to control SRM. For example, the vector control scheme commonly used in the ac motor drives was adopted to control a three-phase SRM [8-9]. However, their objectives were mainly for torque ripple reduction and not radial force control. Another sinusoidal excitation scheme has been proposed to separately control the motor torque and radial force for conventional one winding per pole 12/8 pole SRM [10]. The control scheme works well when both the torque and force are large. However, determining the currents that will produce the desired torque and radial force is cumbersome and limited when a small motor torque is requested.

Recently, an alternative decoupling scheme for torque and radial force control was proposed for conventional 12/8 pole SRM [11]. Motor torque is controlled with the conventional method, i.e. all of the poles in the conduction phase are excited with the same current to produce the desired torque. Two extra poles from the descending inductance phase are excited to produce the required radial force. Although this scheme can effectively produce radial force, the force vector has significant error in both magnitude and orientation due to the exclusion of mutual inductance in the control model. In this paper, a radial force control scheme with similar pole selection strategy for 12/8 pole SRM is presented. Mutual inductances between stator poles are modeled and included in the controller. The production of torque and radial force are decoupled to simplify the controls.

II. TORQUE AND RADIAL FORCE MODEL

Figure 1 shows the schematic of a 12/8-pole switched reluctance motor. The twelve stator pole currents are controlled independently. Only the phase *A* windings are shown. The pole currents are designated as i_{A1} , i_{A2} , i_{A3} , and i_{A4} , respectively, and θ_r is the rotor angle in a conduction period. The aligned position is defined as $\theta_r = 0^\circ$. Because the motor stroke angle is 15 mechanical degrees ($^\circ\text{M}$), with no advancement θ_r is between -15°M to 0°M for motor operation. Consider the attraction force produced at pole *A1* first. A schematic illustrating this force is shown in Fig. 2. The magnetic flux passes through the overlapped area and the non-overlapped area due to fringing. The inductance can be modeled as [12]

$$L_A = \frac{\mu_0 N^2 DR}{g} (\theta_o + K_{fr}) \quad (1)$$

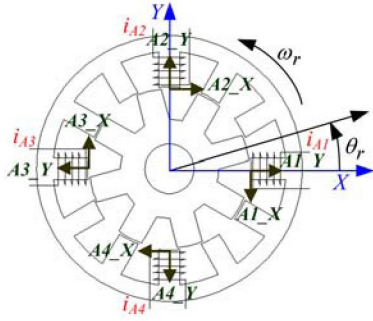


Figure 1. Schematic and coordinate systems of the 12/8 pole SRM.

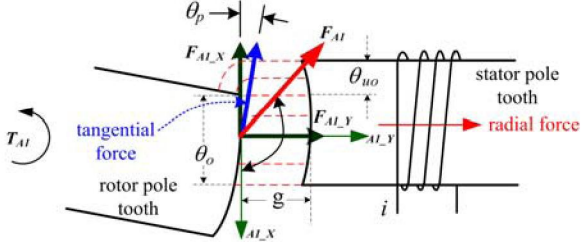


Figure 2. Attraction force produced by pole $A1$.

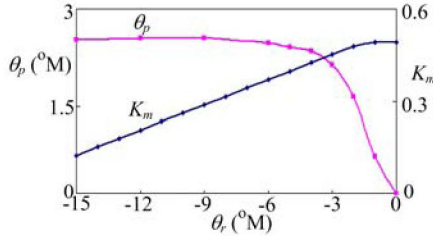


Figure 3. The relationship between θ_p and θ_r .

where μ_o is the permeability of air, K_{fr} is a constant for the fringing inductance, N is the number of turns, D is the stack length, R is the rotor radius, g is the air gap length, θ_o and θ_{uo} are the overlapped and the non-overlapped angles, respectively. Because θ_o and θ_{uo} are simple functions of θ_r , the inductance can be calculated with Eq. (1) easily. The air gap length is assumed uniform in the analysis below. Except for the aligned position, the attraction force between the stator and the rotor tooth is not parallel to the stator pole. A coordinate system is attached on each stator pole to assist the attraction force analysis. For example, the phase A coordinate systems shown in Fig. 1, $A1_Y \sim A4_Y$ are the parallel and $A1_X \sim A4_X$ are the perpendicular axes, respectively, with reference to their corresponding stator pole. The origin is located at the center of the overlapped rotor pole area.

A. Single Pole Excitation

As shown in Fig. 2, let the amplitude and angle of the attraction force for pole $A1$ be F_{A1} and θ_ϕ , respectively, from Eq. (1) F_{A1} can be approximated as

$$F_{A1} = K_F i_{A1}^2 \quad (2)$$

where $K_F = L_A/4g$. Note that F_{A1} is proportional to square of the pole current and varies with θ_r since L_A is a function of the rotor angle. The angle of F_{A1} equals 90 degree when the rotor and the stator poles are aligned, but deviate from 90 degree due to the fringing flux at the non-overlapped area

when the poles are not aligned. The deviation angle can be found by treating the forces produced at the overlapped and non-overlapped areas as independent and concentrated forces [10]. Therefore, the angle of the attraction force can be approximated as,

$$\theta_\phi = 90^\circ + \frac{\theta_{uo}}{\theta_o + K_{fr}} K_{ang} \quad (3)$$

where K_{ang} is a constant. Note that θ_{uo} is positive when the rotor is in the ascending inductance region and negative when in the descending inductance region. The last term in Eq. (3) is the angle due to the fringing flux.

The perpendicular and the parallel force component with respect to the pole $A1$ tooth can be expressed respectively as

$$F_{A1_X} = F_{A1} \cos \theta_\phi \quad (4)$$

$$F_{A1_Y} = F_{A1} \sin \theta_\phi \quad (5)$$

Where F_{A1_Y} is the radial force produced by pole $A1$. The rotor torque, however, cannot be calculated from Eq. (4) directly because F_{A1_X} is not tangential to the rotor pole tooth. As shown in Fig. 2, F_{A1_X} deviates from the tangent of the rotor pole slightly. Let the deviation angle be θ_p . The torque then produced by pole $A1$ can be written as

$$T_{A1} = -F_{A1} \cos(\theta_\phi + \theta_p) R \quad (6)$$

Note that θ_p is a non-linear function of rotor position and is difficult to describe mathematically. Figure 3 shows the relationship between θ_p and θ_r calculated with a finite-element (FE) analysis software. The parameters of the SRM used in the analysis can be found in Appendix A. It can be seen that θ_p is about $2.5^\circ M$ for $\theta_r < -3^\circ M$, and decrease rapidly as θ_r approach the aligned position.

B. Two and Four Poles Excitation

When more than one pole in a phase is excited the mutual inductance between these poles must be considered for accurate radial force and torque modeling. In the following analysis it is assumed that an even number of poles, adjacent to one another, are energized. For simplicity, let poles $A1$ and $A2$ be excited. The attraction forces can then be expressed respectively as [13]

$$F_{A1} = K_F (i_{A1}^2 + K_{mA} i_{A1} i_{A2}) \quad (7)$$

$$F_{A2} = K_F (i_{A2}^2 + K_{mA} i_{A1} i_{A2}) \quad (8)$$

where K_{mA} is a rotor angle dependent term, its relationships with θ_r is also shown in Fig. 3. F_{A1} and F_{A2} can be resolved into an X - and Y -direction force with equations similar to Eqs. (4)-(5). The net torque produced by these two poles is

$$T_{A1,2} = -K_F \cos(\theta_\phi + \theta_p) R (i_{A1}^2 + i_{A2}^2 + 2K_{mA} i_{A1} i_{A2}) \quad (9)$$

In the case when all the poles in a phase are excited, since it is similar to the excitation of two pairs of adjacent poles, the radial force and torque produced by each pole pair can be found with Eqs. (7)-(9) separately. The net force and torque are the sum of the force and torque produced by each pole pairs.

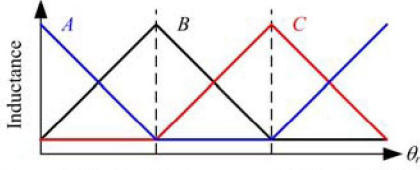


Figure 4. Idealized inductance of 12/8-pole SRM.

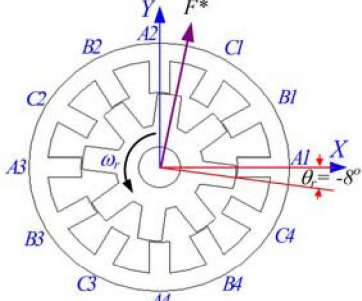


Figure 5. Schematic of the SRM when phase A is the conduction phase and B1, B2 are the radial force producing poles

Table 1 Selection of force control poles

Eqs. (12)(13)	conduction phase	excitation poles
$Q_{cos} > 0, Q_{sin} > 0$	A	B1, B2
	B	C1, C2
	C	A1, A2
$Q_{cos} < 0, Q_{sin} > 0$	A	B2, B3
	B	C2, C3
	C	A2, A3
$Q_{cos} < 0, Q_{sin} < 0$	A	B3, B4
	B	C3, C4
	C	A3, A4
$Q_{cos} > 0, Q_{sin} < 0$	A	B4, B1
	B	C4, C1
	C	A4, A1

C. Radial Force and Torque of the Motor

Under the assumption that even number and adjacent poles are energized in any phase, the net radial forces and torque produced by the SRM can be found and expressed as the following system equations:

$$\begin{bmatrix} F_X \\ F_Y \\ T \end{bmatrix} = \begin{bmatrix} \bar{K}_{X_A} & \bar{K}_{X_B} & \bar{K}_{X_C} \\ \bar{K}_{Y_A} & \bar{K}_{Y_B} & \bar{K}_{Y_C} \\ \bar{K}_{T_A} & \bar{K}_{T_B} & \bar{K}_{T_C} \end{bmatrix} \begin{bmatrix} \bar{I}_A \\ \bar{I}_B \\ \bar{I}_C \end{bmatrix} \quad (10)$$

where F_X and F_Y are the net X- and Y-direction radial force, respectively, T is the net torque, \bar{K} matrices are rotor angle related and are shown in Appendix B, and the current vectors are

$$\bar{I}_P = \begin{bmatrix} i_{P1}^2 + K_{mP} \cdot i_{P1} \cdot (i_{P4} \text{ or } i_{P2}) \\ i_{P2}^2 + K_{mP} \cdot i_{P2} \cdot (i_{P1} \text{ or } i_{P3}) \\ i_{P3}^2 + K_{mP} \cdot i_{P3} \cdot (i_{P2} \text{ or } i_{P4}) \\ i_{P4}^2 + K_{mP} \cdot i_{P4} \cdot (i_{P3} \text{ or } i_{P1}) \end{bmatrix}, \text{ where } P = A, B, C \quad (11)$$

Note that Eq.(10) is a general expression for the relationship between pole currents, torque and radial force produced by the motor. It shows that F_X , F_Y and T can be manipulated with the proper selection of pole currents at any rotor angle. However, given the desired F_X , F_Y and T , there are 12

unknown currents to be determined from only three equations. This means that there are an infinite number of current combinations that yield the desired F_X , F_Y and T . In the next section, a control scheme that requires only three unknown currents is presented, Eq. (10) yields a unique solution with this scheme.

III. RADIAL FORCE CONTROL

Figure 4 shows the idealized phase inductance profile of the 12/8 pole SRM. It can be seen that at any rotor angle there is one phase with ascending inductance, one phase with descending inductance, and one phase with the inductance is at its lowest level. In the conventional SRM control, the ascending-inductance phase is the conduction phase and its poles are excited to produce the desire torque. The low-inductance phase does not produce any useful torque or force. Excitation of the descending-inductance phase produces radial force and negative torque. In the proposed control scheme, motor torque is controlled with the conventional method, i.e. excitation of all the poles in the ascending-inductance phase with the same current, and the desired radial force is produced by two poles in the descending-inductance phase.

Using the condition shown in Fig. 5 as an example, where F^* is the desired radial force vector. At this position phase A is the ascending-inductance phase, phase B is the descending-inductance phase, and phase C is the low-inductance phase for the motor to rotate in the CCW direction. Therefore, poles A1-A4 are excited with same current to produce the desired torque, and pole B1 and B2 are excited to produce the desired radial force. Because B1 and B2 also produce a negative torque, motor torque must be compensated to correct this effect.

A. Selection of Force Control Poles

According to the direction of the desired radial force, two poles of the descending-inductance phase are selected to produce the force. Because the radial forces produced by these poles are 90° M from each other, the two poles adjacent to the desired force vector are selected. Again, the example shown in Fig. 5, $\angle F^*$ is about 75° M, θ_r is -8° M, therefore pole B1 and B2 are selected to produce F^* . To automate the pole selection procedures the following terms relating to the force angle are computed,

$$Q_{cos} = \cos(\angle F^* - \theta_{\text{offset}} + K_{ang} \cdot \theta_{uo} / (\theta_o + K_{fr})) \quad (12)$$

$$Q_{sin} = \sin(\angle F^* - \theta_{\text{offset}} + K_{ang} \cdot \theta_{uo} / (\theta_o + K_{fr})) \quad (13)$$

where θ_{offset} equals 0, 30, and 60° M when the conduction phase is C, A and B phase, respectively, and $K_{ang} \theta_{uo} / (\theta_o + K_{fr})$ is the last term in Eq. (3). Table 1 shows the excitation poles for various rotor angle and conduction phase. In the table, Q_{sin} , Q_{cos} and the conduction phase are used to determine the force control poles.

B. Calculate Force Control Currents

After the force control poles are determined, the currents for these poles can be calculated. Let α and β be the conduction phase and the force control phase, respectively,

the current that produces the required torque be i_T^* , and the currents for the force control be i_{F1}^* and i_{F2}^* , respectively. By applying the above control law Eq. (10) can be simplified into the following 3x3 system equations,

$$\begin{bmatrix} F_X^* \\ F_Y^* \\ T^* \end{bmatrix} = \begin{bmatrix} 0 & \sin(\theta_{\phi\beta} + \theta_{\text{offset}}) & \cos(\theta_{\phi\beta} + \theta_{\text{offset}}) \\ 0 & -\cos(\theta_{\phi\beta} + \theta_{\text{offset}}) & \sin(\theta_{\phi\beta} + \theta_{\text{offset}}) \\ -4\cos(\theta_{\phi\alpha} + \theta_{p\alpha})R & \cos(\theta_{\phi\beta} + \theta_{p\beta})R & \cos(\theta_{\phi\beta} + \theta_{p\beta})R \end{bmatrix} \begin{bmatrix} K_{F\alpha}(1+K_{m\alpha})i_T^{*2} \\ K_{F\beta}(i_{F1}^{*2} + K_{m\beta}i_{F1}^*i_{F2}^*) \\ K_{F\beta}(i_{F2}^{*2} + K_{m\beta}i_{F2}^*i_{F1}^*) \end{bmatrix} \quad (14)$$

where $\theta_{\phi\alpha}$, $\theta_{\phi\beta}$, $\theta_{p\alpha}$ and $\theta_{p\beta}$ are the θ_ϕ and θ_p angles for phase α and β , respectively, and F_X^* , F_Y^* and T^* are the desired radial force components and torque, respectively. The force and torque in Eq. (14) can be separately expressed as the following two equations:

$$\begin{bmatrix} F_X^* \\ F_Y^* \end{bmatrix} = \begin{bmatrix} \sin(\theta_{\phi\beta} + \theta_{\text{offset}}) & \cos(\theta_{\phi\beta} + \theta_{\text{offset}}) \\ -\cos(\theta_{\phi\beta} + \theta_{\text{offset}}) & \sin(\theta_{\phi\beta} + \theta_{\text{offset}}) \end{bmatrix} \begin{bmatrix} K_{F\beta}(i_{F1}^{*2} + K_{m\beta}i_{F1}^*i_{F2}^*) \\ K_{F\beta}(i_{F2}^{*2} + K_{m\beta}i_{F2}^*i_{F1}^*) \end{bmatrix} \quad (15)$$

and

$$T^* = R[-4\cos(\theta_{\phi\alpha} + \theta_{p\alpha}) \cos(\theta_{\phi\beta} + \theta_{p\beta})] \begin{bmatrix} K_{F\alpha}(1+K_{m\alpha})i_T^{*2} \\ K_{F\beta}(i_{F1}^{*2} + i_{F2}^{*2} + 2K_{m\beta}i_{F1}^*i_{F2}^*) \end{bmatrix} \quad (16)$$

Inverting Eq. (15) yields

$$\begin{bmatrix} i_{F1}^{*2} + K_{m\beta}i_{F1}^*i_{F2}^* \\ i_{F2}^{*2} + K_{m\beta}i_{F2}^*i_{F1}^* \end{bmatrix} = \begin{bmatrix} \sin(\theta_{\phi\beta} + \theta_{\text{offset}}) & -\cos(\theta_{\phi\beta} + \theta_{\text{offset}}) \\ \cos(\theta_{\phi\beta} + \theta_{\text{offset}}) & \sin(\theta_{\phi\beta} + \theta_{\text{offset}}) \end{bmatrix} \begin{bmatrix} \frac{F_X^*}{K_{F\beta}} \\ \frac{F_Y^*}{K_{F\beta}} \end{bmatrix} \quad (17)$$

Because $K_{m\beta}$, $\theta_{\phi\beta}$, θ_{offset} , and $K_{F\beta}$ are functions of θ_r , i_{F1}^* and i_{F2}^* can be calculated from F_X^* and F_Y^* with simple algebraic calculations and tables.

C. Calculate Compensation Torque

Equation (16) shows that the force control currents i_{F1}^* and i_{F2}^* also produce a negative motor torque. Designate the torque as ΔT , then from Eq.(16) ΔT can be written as

$$\Delta T = K_{F\beta}R\cos(\theta_{\phi\beta} + \theta_{p\beta}) \left(i_{F1}^{*2} + i_{F2}^{*2} + 2K_{m\beta}i_{F1}^*i_{F2}^* \right) \quad (18)$$

This torque represents the coupling effect between the radial force producing poles and the motor torque. It can be decoupled by adding ΔT to the motor torque command. More on this compensation scheme is given in Section V. Also note that ΔT is typically very small in comparison to the rated torque of the motor since a small i_{F1}^* and i_{F2}^* can produce a very large radial force.

IV. VERIFICATION WITH FINITE ELEMENT ANALYSIS

Figures 6-9 show the FE verification results with the above radial force production scheme. In all figures the SRM was stationary and was commanded to produce a rotating radial force. No load torque was applied except in Fig. 9. Figure 6(a) and (c) show the calculated force and pole A3 current, respectively, when $|F^*|$ was set to various values. Figure 6(b) shows the pole currents of phase A when $|F^*|$ was set to 10N. Note that the B and C pole currents are all zero in this case. It can be seen that at any instant only two poles were excited to produce the radial force. The

radial force was close to being circular as expected.

Figure 7 shows the calculated radial force and i_{A3} when $|F^*|$ was set 15N and θ_r varied from 0° to 14° , the other pole currents are not shown in the figure since their waveforms are similar to i_{A3} except the phase shift. It can be seen that the force errors are very small in all the cases. The current also increased for larger θ_r . The worst case occurred when $\theta_r = 14^\circ$ because the rotor was very close to the unaligned position for the force producing poles (phase A). Note that as mentioned before, θ_r is defined within the conduction phase and is generally negative. However, it is extended to above 0° for better interpretation of the verification results.

Figure 8(a) shows the compensation torque calculated with Eq.(18) for the same conditions as in Fig. 7. Figure 8(b) shows the net motor torque SRM produced after ΔT was compensated. Note that ΔT calculated with Eq.(18) are quite accurate for $\theta_r = 0^\circ$ and 7° , but has slight error for $\theta_r = 14^\circ$. This indicates that the torque produced by the force control poles can be decoupled in general; however, error emerges when the force control phase is in the vicinity of its unaligned position. Figure 9 shows the calculated radial force for $\theta_r = 7^\circ$, $|F^*| = 15$ N, $\angle F^*$ varied from 0 to 360° , and i_T^* was set to 1A, 2A and 3A, respectively, the corresponding load torques are 0.1, 0.4, and 0.9Nm. It can be seen that the variation of load torque have very little influence on the produced radial force.

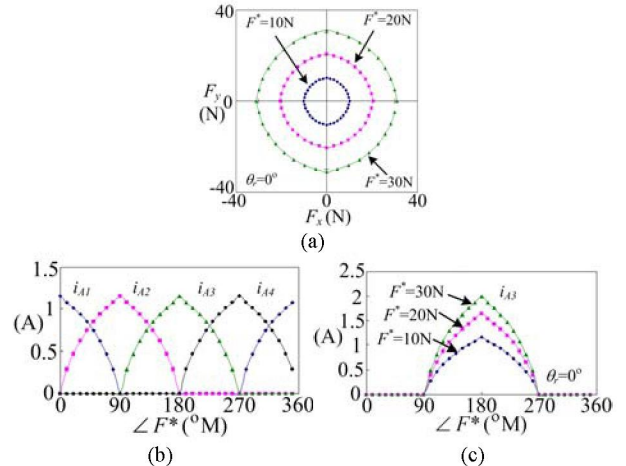


Figure 6. Motor radial force calculated with FE, $\theta_r = 0^\circ$, $|F^*| = 10$ N, 20N, 30N, respectively, no load, $\angle F^*$ varied from 0 to 360° , (a) radial force vector, (b) i_{A1} - i_{A4} , when $|F^*| = 10$ N, (c) i_{A3} for various $|F^*|$.

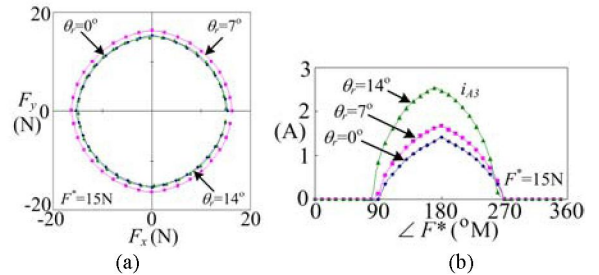


Figure 7. Motor radial force calculated with FE, $|F^*| = 15$ N, $\theta_r = 0^\circ, 7^\circ, 14^\circ$, respectively, no load, $\angle F^*$ varied from 0 to 360° , (a) radial force vector, (b) i_{A3} for various θ_r .

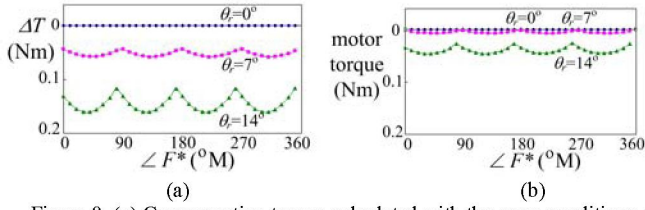


Figure 8. (a) Compensation torque calculated with the same conditions as shown in Fig.7, (b) motor torque after compensation.

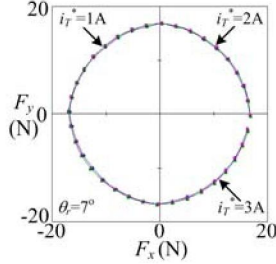


Figure 9. Radial force calculated with FE, $|F^*|=15\text{N}$, $\angle F^*$ varied from 0 to 360° , $\theta_r = 7^\circ$, and $i_r^* = 1\text{A}$, 2A and 3A , respectively.

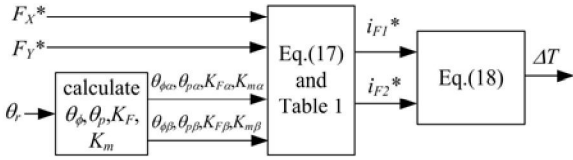


Figure 10. Calculate i_{F1}^* , i_{F2}^* and ΔT from F_x^* , F_y^* and θ_r .

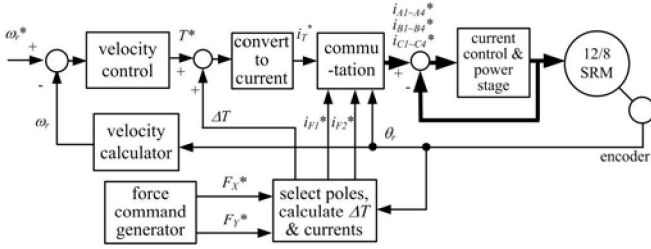


Figure 11. Block diagram of the control system.

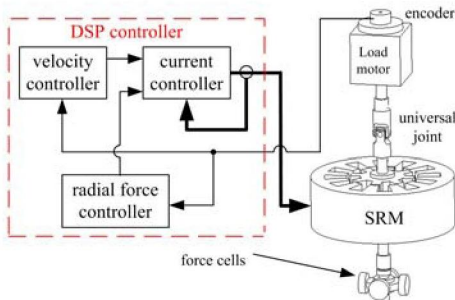


Figure 12. Experimental setup.

V. CONTROL SYSTEM

Figure 10 summarizes the calculation procedures for i_{F1}^* , i_{F2}^* and ΔT . The subscript α and β are referring to the conduction phase and the force control phase, respectively. In the figure, the rotor angle related parameters: θ_α , θ_β , $K_{F\alpha}$, and K_m , are pre-calculated with FE analysis and experiments, and then transformed into appropriate formats and stored as look-up-tables in the controller. Also note that the constants

$K_{F\beta}$ in Eq.(1) and K_{ang} in Eq.(3) are also identified with FE analysis.

A block diagram for the radial force control scheme is shown in Fig. 11. The motor speed is regulated with a PI controller, and the output is the desired torque command T^* . The sum of T^* and the compensation torque ΔT is the net torque command for the motor, this command is then converted to the current command for the conduction phase i_r^* . The desired X - and Y -direction radial force, i.e. F_x^* and F_y^* , are generated according to the needs of the application. Rotor position θ_r is used to determine the ascending-inductance and the descending-inductance phase. All the poles in the ascending-inductance phase are energized with i_r^* . Two poles in the descending-inductance phase are selected using the procedures described in Section III and Table 1, and then energized with i_{F1}^* and i_{F2}^* , respectively. i_{F1}^* and i_{F2}^* are calculated with the procedures shown in Fig.10. The compensation torque ΔT is also calculated in the process.

VI. EXPERIMENTAL RESULTS

The control scheme presented in the previous sections was verified experimentally. The parameters of the SRM are shown in Appendix A. Figure 12 shows the experimental setup. The stator was placed vertically on a platform. The upper end of the rotor was connected to the housing via a universal joint and a bearing. An ac motor was mounted on top of the rotor shaft to provide load to the SRM. Four load cells were mounted on the lower end of the rotor to measure the radial force produced by the motor. Each pole winding has its own current control loop. A DSP was used to perform all of the current, speed, and radial force controls. Hysteresis control action was used for current controllers, and the execution rate was set to about 18.4 kHz. The execution rate of the speed and radial force control was 4.6 kHz. The phase switching angle was advanced 1°M in order to avoid force control at 15°M since at this position the available force is much smaller than the aligned position. Therefore, the torque and force control regions are $-16 \sim -1^\circ\text{M}$ and $-1 \sim 14^\circ\text{M}$, respectively. Note that since the compensation torque is very small near $\theta_r = 0^\circ\text{M}$, advancing the switching angle has very little impact on the overall control strategy.

Figure 13 shows the measured radial force vector and pole $A1 \sim A4$ currents when the motor was at standstill, $\theta_r = 0^\circ\text{M}$, $|F^*| = 10\text{N}$, no load, and $\angle F^*$ varied from 0 to 360° . It can be seen that the force vector was very close to a circle with the magnitude approximately 10N. The pole currents were almost sinusoidal, and at angle instant only two poles were energized. Figure 14 compares the radial force when the mutual inductance in Eq.(17) was included/not included in the calculations, $|F^*|$ was set to 15N. The terms involving multiplication of different pole currents in Eq. (17) were set to zero when the mutual inductance was not considered. It can be seen that significant error existed when the mutual inductance was not included in the calculation.

Figure 15 compares the radial force and i_{A3} current for various θ_r . Figure 15(a) and (b) show the radial force vector

for $\theta_r = 7^\circ\text{M}$ and 14°M , respectively, the radial force for $\theta_r = 0^\circ\text{M}$ was already shown in Fig. 14. It can be seen that the produced force for all θ_r were quite accurate. Figure 15(c) shows that the required pole current became larger as the rotor angle moved near the unaligned position. These are consistent with the FE calculation results shown in Fig. 7.

Figure 16 shows the measured radial force and pole $A1\sim A4$ currents when the motor was running at 100 rpm under 0.5Nm load torque and $|F^*|$ set to: (a) 0N, (b) 10N and rotating synchronously with the rotor, (c) 10N and rotating at 1 Hz. It can be seen in Fig. 16(a) that the pole currents were pulses with approximately the same amplitude. This is identical to a conventional current controlled SRM since zero radial force was commanded. The measured force vectors were significantly smaller in comparison to the forces when $|F^*|$ was set to 10N. In Figs. 16(b) and (c), however, part of the current pulses carried currents at the descending-inductance region to produce radial force. The radial force vectors were circular but with noticeable ripples. As shown in Fig. 16(b), the force ripple appeared at approximately the same directions. Also, the force oscillated about twelve times per revolution. Because the force command was synchronous with the rotor, the force producing poles happened to commutating between the following two cases: 1) force command was located near one of the force poles, and 2) force command was at the vicinity of the center of the force poles. Since the K_m used in the model has slight error, the actual force produced in case 2) was larger than the force produced in case 1) for the same K_m . As a result, the force contained twelve ripples in each revolution. Note that as shown in Fig. 16(c), the above phenomenon on force ripple did not occur when the radial force was rotating at 1Hz, which was asynchronous to the rotor speed. Despite the ripple, the average radial force produced were approximately 10N as commanded.

Figure 17 and 18 show the measured radial force vectors under the same operating conditions as that in Fig. 16 except the motor was running at 600 and 1000rpm, respectively. Similar results were obtained when zero radial force was commanded. On the other hand, it can be seen that the force ripples in Fig. 17(b) became slightly larger and more noticeable when comparing to the synchronous force waveforms shown in Fig. 16(b). The ripple patterns were similar in these figures since the radial force was synchronous to the rotor. However, as shown Fig. 18(b), force ripple reduced significantly when the motor was running at 1000rpm. This is because the radial force was measured through the force cells located at the lower end of the rotor shaft. The rotor and shaft structure was a low pass filter to the measured shaft radial force. Note also that the shape of the force was slightly oval. This is caused mainly by the air gap eccentricity produced by the motor manufacturing process. Regardless of the radial force frequency the eccentric air gap caused similar distortions in the radial force waveforms. Also, as shown in Fig. 17(c) and 18(c), due to this ovalisation effect the force ripple no longer appeared at the same directions when the radial force was not synchronous to the rotor.

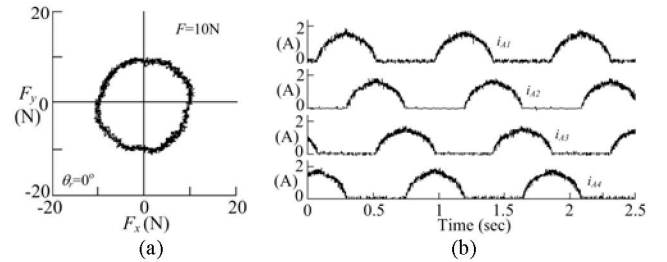


Figure 13. Radial force and pole $A1\sim A4$ currents when the SRM was at standstill, $\theta_r = 0^\circ\text{M}$, $|F^*| = 10\text{N}$, no load, and $\angle F^*$ varied from 0 to 360° , (a) radial force vector, (b) pole $A1\sim A4$ currents.

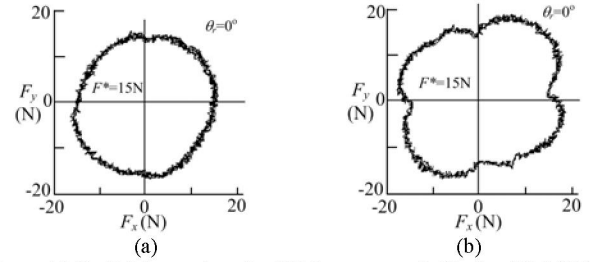


Figure 14. Radial force when the SRM was at standstill, $\theta_r = 0^\circ\text{M}$, $|F^*| = 15\text{N}$, no load, and $\angle F^*$ varied from 0 to 360° , (a) included, and (b) not included the mutual inductance.

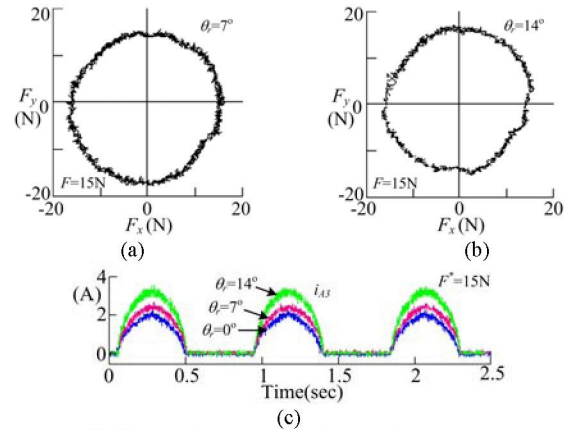


Figure 15. Radial force and i_{A3} current and when the SRM was at standstill, $|F^*| = 15\text{N}$, $\angle F^*$ varied from 0 to 360° , (a) radial force when $\theta_r = 7^\circ\text{M}$, (b) radial force when $\theta_r = 14^\circ\text{M}$, (c) i_{A3} for various θ_r .

VII. CONCLUSIONS

A scheme to produce controlled radial force in a 12/8-pole SRM was proposed in this paper. The twelve stator pole currents are controlled independently. The motor torque was controlled using the conventional method, i.e. all poles in the conduction phase are excited with the same current to produce the desired torque. Two additional poles from the descending-inductance phase were energized to produce the required radial force. Because the force producing poles also produce a negative torque, this torque was compensated so that the motor output torque and radial force controls are decoupled. The motor parameters needed for the control were obtained from the finite-element analysis of the SRM, and then stored as lookup-tables in the controller. In general, the accuracy of the parameters obtained with FE analysis was adequate for the control scheme. The experimental results show that when controlled with the proposed scheme, the SRM was able to produce a

controlled radial force when at standstill or running, and subjected to a load torque. Although the radial forces exhibited noticeable ripples caused by the commutation of the force producing poles, their averages were very close to the command values.

A possible application of this scheme is to produce the radial force required to cancel the forces produced by ϵ non-uniform air gap or external load, and thereby reduce the SRM vibrations. Because the objective of this paper is on the development of a radial force control scheme, generation of appropriate commands to cancel the defect-induced radial forces is not discussed. However, the command generation algorithm is required for the successful application of this scheme.

APPENDIX A

The 12/8 pole SRM used in this paper is 100 Watts, 1000 rpm, 3Amp. Aligned inductance = 8 mH, un-aligned inductance = 2 mH, $K_{ang} = 4.1$, $K_{fr} = 3.1$.

APPENDIX B

$$\begin{aligned} \bar{K}_{X_A} &= K_{FA} [\sin(\theta_{\phi A}) \cos(\theta_{\phi A}) - \sin(\theta_{\phi A}) - \cos(\theta_{\phi A})] \\ \bar{K}_{Y_A} &= K_{FA} [-\cos(\theta_{\phi A}) \sin(\theta_{\phi A}) \cos(\theta_{\phi A}) - \sin(\theta_{\phi A})] \\ \bar{K}_{T_A} &= -K_{FA} [\cos(\theta_{\phi A} + \theta_{pA}) \cos(\theta_{\phi A} + \theta_{pA}) \cos(\theta_{\phi A} + \theta_{pA}) \cos(\theta_{\phi A} + \theta_{pA})] \\ \bar{K}_{X_B} &= K_{FB} [\sin(\theta_{\phi B} + 30) \cos(\theta_{\phi B} + 30) - \sin(\theta_{\phi B} + 30) - \cos(\theta_{\phi B} + 30)] \\ \bar{K}_{Y_B} &= K_{FB} [-\cos(\theta_{\phi B} + 30) \sin(\theta_{\phi B} + 30) \cos(\theta_{\phi B} + 30) - \sin(\theta_{\phi B} + 30)] \\ \bar{K}_{T_B} &= -K_{FB} [\cos(\theta_{\phi B} + \theta_{pB}) \cos(\theta_{\phi B} + \theta_{pB}) \cos(\theta_{\phi B} + \theta_{pB}) \cos(\theta_{\phi B} + \theta_{pB})] \\ \bar{K}_{X_C} &= K_{FC} [\sin(\theta_{\phi C} + 60) \cos(\theta_{\phi C} + 60) - \sin(\theta_{\phi C} + 60) - \cos(\theta_{\phi C} + 60)] \\ \bar{K}_{Y_C} &= K_{FC} [-\cos(\theta_{\phi C} + 60) \sin(\theta_{\phi C} + 60) \cos(\theta_{\phi C} + 60) - \sin(\theta_{\phi C} + 60)] \\ \bar{K}_{T_C} &= -K_{FC} [\cos(\theta_{\phi C} + \theta_{pC}) \cos(\theta_{\phi C} + \theta_{pC}) \cos(\theta_{\phi C} + \theta_{pC}) \cos(\theta_{\phi C} + \theta_{pC})] \\ K_{FA} &= L_A / 4g, K_{FB} = L_B / 4g, K_{FC} = L_C / 4g \end{aligned}$$

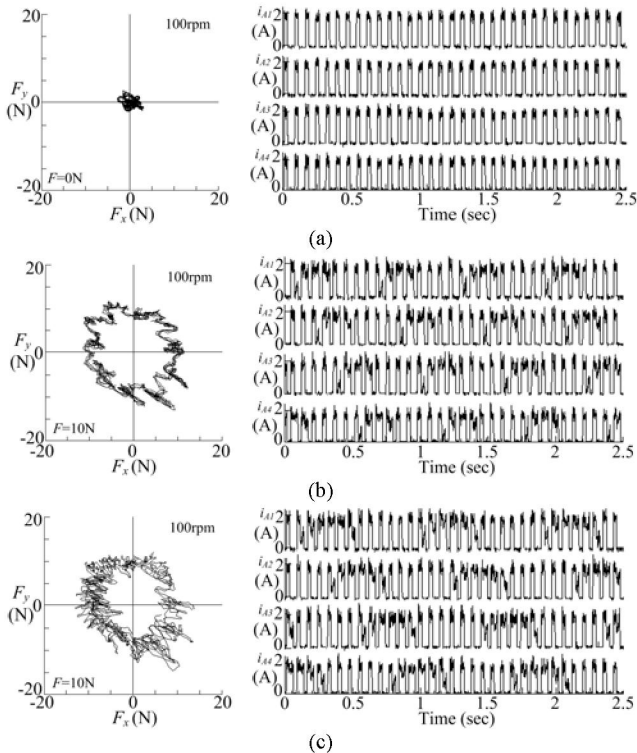


Figure 16. Radial force vector and pole A1~A4 currents when the motor was running at 100 rpm under 0.5 Nm load torque and $|F^*|$ set to: (a) 0N, (b) 10N and rotating synchronously with the rotor, (c) 10N and rotating at 1 Hz.

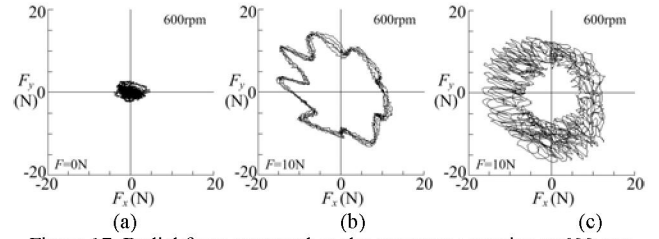


Figure 17. Radial force vector when the motor was running at 600 rpm under 0.5Nm load torque and $|F^*|$ set to: (a) 0N, (b) 10N and rotating synchronously with the rotor, (c) 10N and rotating at 1 Hz.

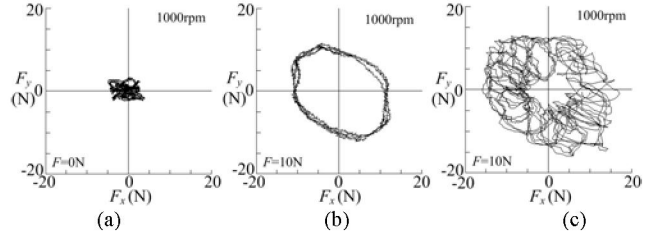


Figure 18. Radial force vector when the motor was running at 1000 rpm under 0.5Nm load torque and $|F^*|$ set to: (a) 0N, (b) 10N and rotating synchronously with the rotor, (c) 10N and rotating at 1 Hz.

ACKNOWLEDGMENT

We gratefully acknowledge the support for this research by the National Science Council, Taiwan, R. O. C., under grant: NSC 94-2213-E-032-028.

REFERENCE

- [1] S. Ayari, M. Besbes, M. Lecrivain, and M. Gabsi, "Effects of the Air gap Eccentricity on the SRM Vibrations", International Conference on Electric Machines and Drives, 1999, pp. 138-140.
- [2] N.R. Garrigan, W.L. Soong, C.M. Stephens, A. Storaice, and T.A. Lipo, "Radial Force Characteristics of a Switched Reluctance Machine", IEEE IAS Annual Meeting, Vol. 4, 1999, pp. 2250-2258.
- [3] I. Husain, A. Radun, and J. Nairus, "Unbalanced Force Calculation in Switched Reluctance Machines", IEEE Trans. on Magnetics, Vol. 36, Jan. 2000, pp. 330-338.
- [4] C. Michioka, T. Sakamoto, O. Ichikawa, A. Chiba, and T. Fukao, "A Decoupling Control Method of Reluctance-Type Bearingless Motors Considering Magnetic Saturation", IEEE IAS Annual Meeting, Vol.1, Oct. 1995, pp. 405-411.
- [5] M. Takemoto, H. Suzuki, A. Chiba, T. Fukao, and M. A. Rahman, "Improved Analysis of a Bearingless Switched Reluctance Motor", IEEE Trans. on Industry Applications, Vol.37, Jan./Feb. 2001, pp. 26-34.
- [6] M. Takemoto, A. Chiba, H. Akagi, and T. Fukao, "Radial Force and Torque of a Bearingless Switched Reluctance Motor Operating in a Region of Magnetic Saturation", IEEE IAS Annual Meeting, Vol. 1, 2002, pp. 35-42.
- [7] M. Takemoto, A. Chiba, T. Fukao, "A Method of Determining the Advanced Angle of Square-Wave Currents in a Bearingless Switched Reluctance Motor", IEEE Trans. on Industry Applications, Vol. 37, Nov./Dec. 2001, pp. 1702-1709.
- [8] N.J. Nagle, and R.D. Lorenz, "Rotating Vector Method for Sensorless, Smooth Torque Control of a Switched Reluctance Motor Drive", IEEE IAS Annual Meeting, Vol.1, Oct. 1998, pp. 723 -730.
- [9] T.H. Liu, Y.J. Chen, and M.T. Lin, "Vector Control and Reliability Improvement for a Switched Reluctance Motor", IEEE International Conference on Industrial Technology, Dec. 1994, pp. 538 -542.
- [10] F. C. Lin and S. M. Yang, "Instantaneous Shaft Radial Force Control with Sinusoidal Excitations for Switched Reluctance Motors", IEEE IAS Annual Meeting, Seattle, Oct. 2004, pp. 424-430.
- [11] W. T. Liu and S. M. Yang, "Modeling and Control of a Self-Bearing Switched Reluctance Motor", IEEE IAS Annual Meeting, Hong Kong, Oct. 2005, pp. 2720-2725.
- [12] G. R. Slemon, *Electric Machines and Drives*, Addison Wesley, 1992.
- [13] B. S. Guru and H. R. Hiziroglu, *Electric Machinery & Transformers*, Oxford, 1995.